Nanometer-Thick Equilibrium Films: The Interface Between Thermodynamics and Atomistics

Mor Baram, *et al.*

Science **332**, 206 (2011);
DOI: 10.1126/science.1201596

Nanometer-Thick Equilibrium Films: The Interface Between Thermodynamics and Atomistics

Mor Baram,[1]* Dominique Chatain,[2] Wayne D. Kaplan[1]†

Nanometer-thick films at interfaces and surfaces exist in various materials and can substantially influence their properties. Whether these films are an equilibrium or transient state is debated. To address this question, we equilibrated 1.2-nanometer-thick films at gold-sapphire interfaces in the presence of anorthite glass and measured the solid-solid interface energy. The equilibrated film significantly reduced the interfacial energy and could be described by the Gibbs adsorption isotherm expanded to include structure in addition to chemical excess. Unlike artificially made conventional thin films, these films do not break up during equilibration and offer an alternative design criterion for thin-film technology. These results demonstrate that nanometer-thick films at interfaces and surfaces can be an equilibrium state and included in phase diagrams with dedicated tie-lines.

Films of ~1-nm thickness at grain boundaries (GBs) in polycrystalline materials, phase boundaries, and free surfaces are ubiquitous. They have been identified at GBs in ceramics, where they limit high-temperature mechanical properties and influence grain growth during sintering, and can be used to engineer functional properties (*1*–*6*). The same type of nanometer-thick film has been identified at the surface of oxides (*7*) and polymers (*8*), including the surface of ice, where a thin (nanometer range) film of water forms, providing the lubricant for ice-skating (*9*), and causes the shifting of petroleum pipes located in northern regions (*10*). More recently, such films have been identified at interfaces between metals and oxides (*11*–*14*) and at GBs in metallic alloys (*15*, *16*). One of the main characteristics of these films is that their thickness and average composition are constant along a particular interface or surface, and they are not considered a bulk phase.

A fundamental question is whether these nanometer length–scale films, which are often called intergranular films (IGFs), are an equilibrium interface state, a wetting film (which is a bulk phase), or a transient phenomenon due to impurities, mass transport, or oxidation (Fig. 1). If they are indeed an equilibrium interface state, then IGFs can potentially be mapped onto bulk phase diagrams as tie-lines, which define the equilibrium state of (two-dimensional) surfaces and interfaces (*17*, *18*). Here, we present an experimental approach to measure interface energy with and without IGFs and show that 1.2-nm-thick IGFs at gold-sapphire interfaces are stable interface states associated with a decrease in excess energy.

Equilibration of gold particles on sapphire in the presence of glass. Gold films (60 nm thick) deposited on sapphire (α-Al_2O_3) basal plane substrates were annealed in air at 1100°C for 2 hours, after the substrates were first partially coated with anorthite glass (CaO-$2SiO_2$-Al_2O_3) droplets (details in Materials and Methods). Anorthite is a source of the elements that are often found in IGFs at alumina grain boundaries (*4*) and metal-alumina interfaces (*11*–*14*), and the presence of bulk anorthite specifically defines the chemical potentials of these elements in our experiments. Due to the finite contact angles of gold on anorthite and sapphire, during thermal annealing the gold film broke up into small particles dispersed on the substrate (Fig. 2A) (*14*). Cross-section transmission electron microscopy (TEM) specimens were prepared using a dual-beam focused ion beam (FIB) system (Fig. 2B) (*19*) and examined by aberration-corrected high-resolution TEM (HRTEM). The results were compared to measurements from specimens prepared by the same process but equilibrated without anorthite glass (*20*).

Morphological characterization of the intergranular film. The interface between gold and sapphire examined by HRTEM showed the presence of a 1.2-nm-thick IGF (Fig. 2C). The film composition was found to include Ca and Si (*14*) but at a different concentration than in anorthite, which together with the finite and constant thickness indicated that this was not a wetting film (Fig. 1). If it were a wetting film (Fig. 1B), the film thickness would have increased as a function of increasing anorthite glass volume in the system, which was not the case. With an IGF, a preferred orientation of the (111) gold plane was found parallel to the sapphire (0001) surface, while no low-index orientation relationship existed between the gold particles and the sapphire (table S1). Without an IGF, both (111) and (200) gold preferred orientations were found parallel to (0001) sapphire, with defined low-index orientation relationships

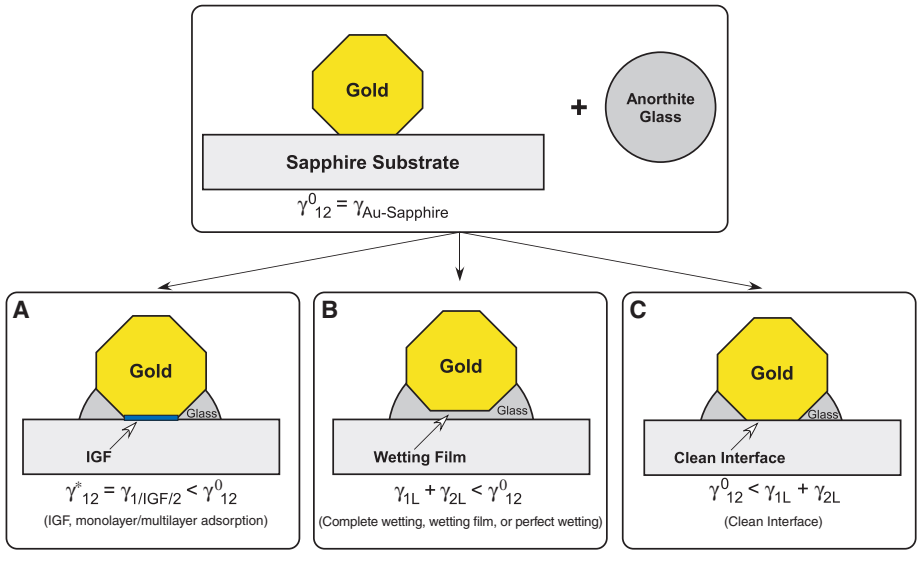

Fig. 1. Schematic drawings of an interface, formed when two bulk phases (gold and sapphire) are equilibrated in the presence of a third phase (bulk anorthite glass). Although the final geometric configuration will minimize the total interface and surface energies (via contact and dihedral angles), the interface between the gold and sapphire can adopt one of the following configurations: (**A**) An intergranular film forms at the interface, which has a lower interface energy than the original gold-sapphire interface; (**B**) a wetting film forms between the gold and sapphire, resulting in two interfaces (1L and 2L) between the sapphire and glass and between the gold and glass; or (**C**) a "clean" interface forms having an energy equivalent to that of the original configuration.

[1]Department of Materials Engineering, Technion–Israel Institute of Technology, Haifa, 32000, Israel. [2]CNRS, Aix-Marseille University, CINAM-UPR3118, campus de Luminy, F-13288 Marseille, France.

*Present address: School of Engineering and Applied Sciences, Harvard University, Cambridge, MA 02138, USA.
†To whom correspondence should be addressed. E-mail: kaplan@tx.technion.ac.il

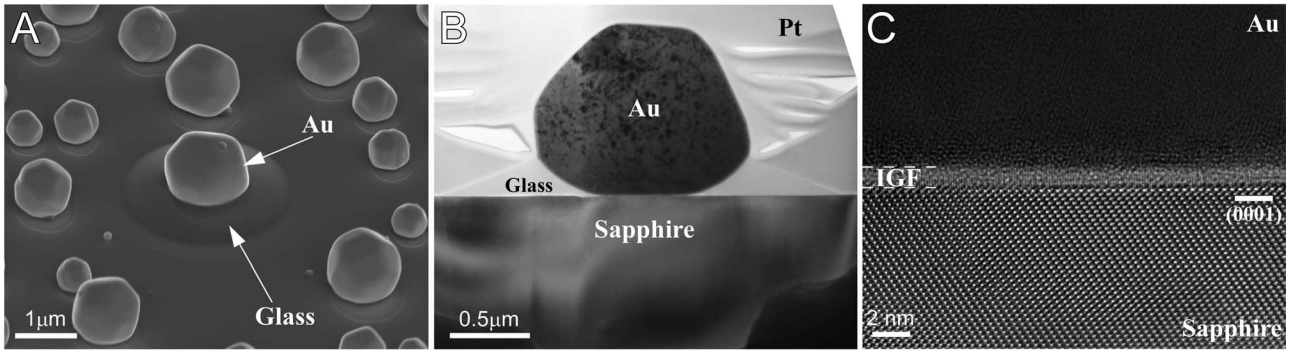

Fig. 2. (**A**) Secondary electron scanning electron micrograph (acquired with the dual-beam FIB) showing a single gold particle located on an anorthite drop. (**B**) Bright-field TEM micrograph of a cross-section TEM specimen prepared from a gold particle on an anorthite drop such as in (A). This specimen was prepared with the FIB "lift out" technique. The contrast above the gold is from the protective Pt coating that was deposited before the FIB "lift-out" process. (**C**) Aberration-corrected HRTEM micrograph (Cs ~ −5 μm) of an equilibrated interface between a gold particle and a basal plane sapphire substrate. A ~1-nm-thick IGF has equilibrated at the interface. The micrograph was recorded after orienting the sapphire in the [1$\bar{2}$10] zone axis.

(*20*, *21*). This indicated that the IGF produced a decrease in the in-plane anisotropy of the gold-sapphire interface energy.

Interface energy measurements. One advantage of equilibrating metal particles in contact with the sapphire substrate at thermodynamic coexistence with bulk anorthite is that the gold-sapphire interface energy can be determined in the presence of an IGF, at controlled chemical potentials. Figure 3 presents a schematic illustration of the geometric configuration of a gold particle that partially resides inside an anorthite droplet on the sapphire substrate. All the relevant surface and interface energies are indicated in Fig. 3, and the experimental contact and dihedral angles are defined in the micrographs presented in Figs. 4 and 5.

From dihedral and contact angle analysis (see table S2 and "Determination of interface energy" in the SOM), a reduction in interface energy of ~190 mJ/m^2 occurs in the presence of the IGF at the gold-sapphire interface, compared to the same interface without an IGF (*20*). Given the potential impurity level of the starting materials used for the analysis conducted in (*20*), monolayer or submonolayer interface adsorption may have occurred, indicating that the interface energy of hypothetically pure gold-sapphire interfaces (without an IGF) is even higher than that reported. An even larger reduction in interface energy is expected if adsorption of the glass constituents to the sapphire and/or gold surfaces has occurred, providing experimental proof for the reduction of the gold-sapphire interface energy in the presence of an IGF. The x-ray diffraction results (table S1) further corroborate these findings, demonstrating a reduction in in-plane interface anisotropy due to the presence of an IGF (resulting in a preferred orientation instead of a low-index orientation relationship, as was mentioned before).

Intergranular films (complexions) and the Gibbs adsorption isotherm versus wetting films. Since the discovery of IGFs, their origin and stability have been debated. It was assumed that IGFs, in a manner similar to that of wetting films, reduce the interfacial energy of a system. Clarke *et al.*

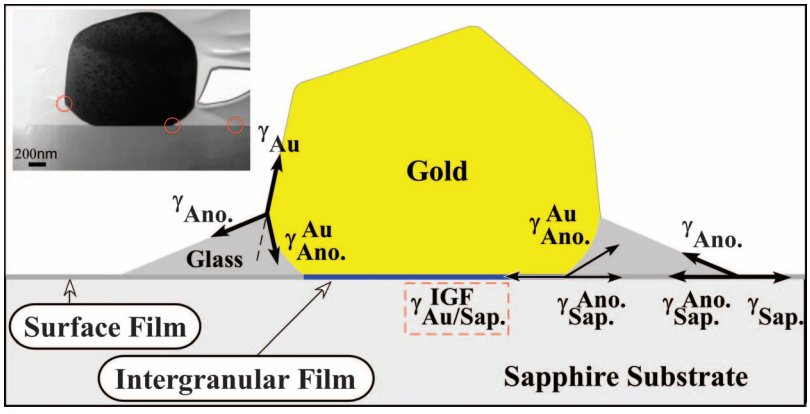

Fig. 3. Schematic drawing of the geometric configuration of the system with a gold particle partially immersed in an anorthite drop. All the relevant surface and interface energies are indicated. The inset (upper left corner) presents a TEM micrograph of a real gold particle on an anorthite droplet, on the sapphire substrate.

(*22*, *23*) extended the wetting film analogy to IGFs by defining two film-crystal interfaces instead of considering only one interface that includes the IGF, as was done in this study. Treating the IGF as a single interface is more correct, because the IGF is not a bulk phase but rather an interface state (*17*, *24*), so its properties differ from those of a bulk wetting film. The reduction in energy due to the existence of IGFs was predicted from general experimental observations and theory (*17*, *22*, *25*, *26*), in that IGFs do not exist at all GBs, but rather exist only at high-angle (high-energy) GBs, causing their energy to be reduced to that of special (low-energy) and/or low-angle GBs (*2*, *22*). In addition, in an extensive study conducted on surface films, it was predicted that the reduction in energy is necessary for stabilization (*27*, *28*). The reduction in interface energy measured in this work confirms these studies.

Dillon *et al.* indirectly compared the relative energies of GBs containing different interface states [called "complexions" by the authors (*18*)] by correlating GB dihedral angles (*29*) with GB mobility (*18*). They found that in some cases, a reduction in energy occurred due to a change of complexion that was inferred from GB mobility measurements. Although it is difficult to compare the relative values averaged for different GBs with the absolute values determined in the present study, the prior work provides evidence that the phenomena reported here occur for a wide variety of complex GB geometries. Yoshiya *et al.* showed from molecular dynamics simulations that the IGF is indeed energetically favorable at Si_3N_4 twist boundaries, where the excess free energy was correlated with the segregation of atoms with dangling bonds at the interface (*30*).

Although various models have been used to address IGFs, they can also be directly defined via the Gibbs adsorption isotherm (*31*)

$$d\gamma = -\sum_i \Gamma_i d\mu_i \qquad (1)$$

where a surface (or interfacial) energy (γ) is reduced by the presence of (surface) interfacial excess (Γ) and a change in chemical potential (μ). The key for applying this isotherm to IGFs is to determine the dividing surface (interface) of Gibbs, which is a mathematical plane between the two phases that contains the interfacial excess. This excess is not necessarily located on one atomic

plane but can be spread over several atomic planes, starting from part of a monolayer and extending up to (but not including) a wetting film. Most of the analytical models (and related experiments) that were developed to obtain the change in surface energy due to adsorption usually ignore the interface structure and consider only the interfacial chemical excess (number of atoms per area, or number of monolayers) (*32*). The local atomistic structure must be included, because IGFs are expected to have some varying order adjacent to the crystals (*33*, *34*) and the degree of order is expected to influence the energy (*35*). Indeed, ordering in liquids adjacent to solids and reconstructed surfaces can be defined as types of complexions (*36*). We have also experimentally confirmed that the IGFs in this study are partially ordered (*37*), and thus the excess (Γ) used to define an IGF must include a description of both the interface chemistry and structure, which can then be correlated with the decrease in interface energy via the Gibbs isotherm.

Diffuse interfaces, van der Waals, and image forces. Since IGFs are an equilibrium state, complexion diagrams (similar to phase diagrams) can be constructed to predict interfacial structure and chemistry, by using phase-field and diffuse interface models (*25*, *38*, *39*) [the latter partially based on Cahn's critical point wetting theory (*40*)]. In these models, in contrast to the approach of Gibbs and Cahn, a function is used to describe the misorientation and structural order of an interface (*41*). One prediction from these models is that partially disordered interface states are more likely to be stable at high-energy GBs than at low-energy GBs [identical to the experimental observations (*22*)].

Force-balance models, based on a balance between various attractive forces (e.g., van der Waals forces) and repulsive forces (e.g., steric forces), have been widely used to describe interfaces with an IGF (*42*). Values of the Hamaker coefficient can be used to estimate attractive London (van der Waals) forces at grain boundaries and interfaces (*43*). Lipkin *et al*. developed a model to assess the contribution of the van der Waals forces to the thermodynamic work of adhesion (W_{ad}) at metal-alumina interfaces without an IGF and calculated a contribution of 330 to 560 mJ/m^2 to the value of W_{ad} (*44*). From comparison to experimental results, they concluded that for gold-alumina interfaces, van der Waals forces are an important contribution to W_{ad}. However, if we perform the same calculation for the attractive London dispersion forces at a gold-sapphire interface with an IGF, we reach the opposite conclusion. Our measured W_{ad} (640 mJ/m^2) is three orders of magnitude higher than the van der Waals contribution (0.94 mJ/m^2), when we use a Hamaker coefficient calculated for the gold-sapphire interface containing an IGF (*14*). Therefore, we conclude that the main IGF contribution to the reduction in interface energy at gold-sapphire interfaces is not a simple van der Waals interaction.

Johnston and Finnis demonstrated that image forces should be considered for the case of metal-oxide interfaces containing an IGF, based on a classical density functional model used to calculate the electrostatic and entropic forces between two planar surfaces separated by a thin (~1-nm) glass film containing a distribution of counterions (*45*). The model was applied to the copper-sapphire interface with an IGF, on the basis of the experimental results for this interface (*11*). It was found that the image interaction force reduces the interface energy by ~100 mJ/m^2, and it dominates over the van der Waals contribution (which was estimated to be 0.149 mJ/m^2). The decrease in interface energy due to image forces is of the same order of magnitude as the experimental decrease in interface energy measured in the present study (~190 mJ/m^2). Therefore, we conclude that image forces are a dominating attractive force at gold-sapphire interfaces containing an IGF.

We have shown here that equilibrating a two-phase system (gold and sapphire) in the presence of a third phase (anorthite) changes the chemical potentials, resulting in Gibbsian adsorption in the form of an IGF. In addition, the IGF has both a specific average composition and structure, which fits with the definition of a complexion (whereby interfaces can adopt states that have distinct interfacial structure and/or composition profiles, correlated with local minima in free energy). Furthermore, this finding can be used to develop grain boundary/interface complexion diagrams (using diffuse interface models). The diagrams may be used to predict the most stable structure and composition, and in combination with experiments, tailor materials with specific macroscopic properties.

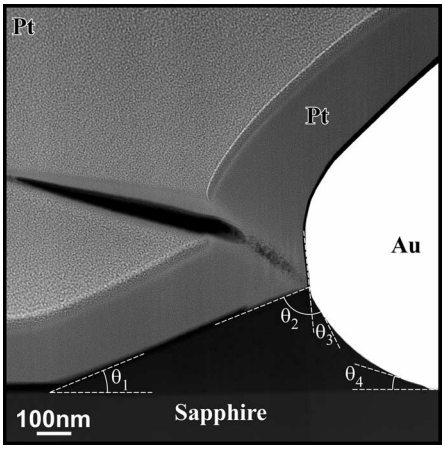

Fig. 4. Dark-field scanning TEM micrograph of the triple junction region, from which the interface energies were measured. All the angles that were used in the measurements are indicated on the micrograph.

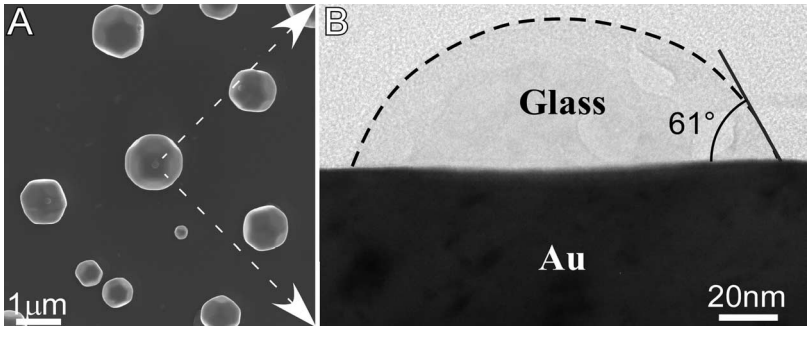

Fig. 5. (**A**) An example of a small glass droplet on a gold particle from which the glass-gold contact angle was determined. A cross-section TEM specimen was prepared from the particle and droplet by FIB. (**B**) A TEM micrograph of the droplet on the Au (100) facet.

References and Notes

1. D. R. Clarke, G. Thomas, *J. Am. Ceram. Soc.* **60**, 491 (1977).
2. H.-J. Kleebe, M. J. Hoffmann, M. Rühle, *Z. Metallk.* **83**, 610 (1992).
3. L. K. L. Falk, *J. Eur. Ceram. Soc.* **17**, 983 (1997).
4. R. Brydson *et al*., *J. Am. Ceram. Soc.* **81**, 369 (1998).
5. Y.-M. Chiang, L. A. Silverman, R. H. French, R. M. Cannon, *J. Am. Ceram. Soc.* **77**, 1143 (1994).
6. M. P. Harmer, *J. Am. Ceram. Soc.* **93**, 301 (2010).
7. H. Qian, J. Luo, *Acta Mater.* **56**, 4702 (2008).
8. G. Decher, *Science* **277**, 1232 (1997).
9. R. Rosenberg, *Phys. Today* **58**, 50 (2005).
10. J. S. Wettlaufer, *Phys. Rev. Lett.* **82**, 2516 (1999).
11. C. Scheu, G. Dehm, W. D. Kaplan, *J. Am. Ceram. Soc.* **84**, 623 (2001).
12. A. Avishai, W. D. Kaplan, C. Scheu, *Z. Metallk.* **94**, 272 (2003).
13. A. Avishai, C. Scheu, W. D. Kaplan, *Acta Mater.* **53**, 1559 (2005).
14. M. Baram, W. D. Kaplan, *J. Mater. Sci.* **41**, 7775 (2006).
15. J. Luo, X. M. Shi, *Appl. Phys. Lett.* **92**, 101901 (2008).
16. V. K. Gupta, D. H. Yoon, H. M. Meyer III, J. Luo, *Acta Mater.* **55**, 3131 (2007).
17. M. Tang, W. C. Carter, R. M. Cannon, *Phys. Rev. B* **73**, 024102 (2006).
18. S. J. Dillon, M. Tang, W. C. Carter, M. Harmer, *Acta Mater.* **55**, 6208 (2007).
19. M. Baram, W. D. Kaplan, *J. Microsc.* **232**, 395 (2008).
20. H. Sadan, W. D. Kaplan, *J. Mater. Sci.* **41**, 5099 (2006).
21. H. J. Fecht, H. Gleiter, *Acta Metall.* **33**, 557 (1985).
22. D. R. Clarke, *Annu. Rev. Mater. Sci.* **17**, 57 (1987).
23. M. P. Brada, D. R. Clarke, *Acta Mater.* **45**, 2501 (1997).
24. J. Luo, *Crit. Rev. Solid State Mater. Sci.* **32**, 67 (2007).
25. C. M. Bishop, M. Tang, R. M. Cannon, W. C. Carter, *Mater. Sci. Eng. A* **422**, 102 (2006).
26. P. Wynblatt, D. Chatain, *Mater. Sci. Eng. A* **495**, 119 (2008).
27. H. Qian, J. Luo, *Appl. Phys. Lett.* **91**, 061909 (2007).
28. H. Qian, J. Luo, Y.-M. Chiang, *Acta Mater.* **56**, 862 (2008).
29. S. J. Dillon, M. P. Harmer, G. S. Rohrer, *J. Am. Ceram. Soc.* **93**, 1796 (2010).
30. M. Yoshiya, I. Tanaka, H. Adachi, R. M. Cannon, *Int. J. Mater. Res.* **101**, 57 (2010).
31. J. W. Gibbs, in *The Scientific Papers of J. Willard Gibbs* (Dover, New York, 1961), vol. 1, pp. 219–331.
32. P. Wynblatt, D. Chatain, *Metall. Mater. Trans. A* **37**, 2595 (2006).

33. G. B. Winkelman *et al.*, *Appl. Phys. Lett.* **87**, 061911 (2005).
34. S. H. Oh, Y. Kauffmann, C. Scheu, W. D. Kaplan, M. Rühle, *Science* **310**, 661 (2005).
35. J. J. Kuna *et al.*, *Nat. Mater.* **8**, 837 (2009).
36. W. D. Kaplan, Y. Kauffmann, *Annu. Rev. Mater. Res.* **36**, 1 (2006).
37. M. Baram, thesis, Technion–Israel Institute of Technology (2010).
38. R. Kobayashi, J. A. Warren, W. C. Carter, *Physica D* **140**, 141 (2000).
39. C. M. Bishop, R. M. Cannon, W. C. Carter, *Acta Mater.* **53**, 4755 (2005).
40. J. W. Cahn, *J. Chem. Phys.* **66**, 3667 (1977).
41. M. Tang, W. C. Carter, R. M. Cannon, *Phys. Rev. Lett.* **97**, 075502 (2006).
42. D. R. Clarke, *J. Am. Ceram. Soc.* **70**, 15 (1987).
43. A. Avishai, W. D. Kaplan, *Acta Mater.* **53**, 1571 (2005).
44. D. M. Lipkin, J. N. Israelachvili, D. R. Clarke, *Philos. Mag. A* **76**, 715 (1997).
45. K. Johnston, M. W. Finnis, *J. Am. Ceram. Soc.* **85**, 2562 (2002).
46. We thank H. Meltzman, P. Wynblatt, and W. C. Carter for fruitful discussions and invaluable comments. This work was supported by the Israel Science Foundation (#163/05) and the Russell Berrie Nanotechnology Institute at the Technion. M.B. acknowledges support from the Israeli Ministry of Science via an Eshkol Fellowship. The research leading to these results has received funding from the European Community's Seventh Framework Programme (FP7/2007-2013) under grant agreement FP7-NMP-2009-CSA-233484.

Supporting Online Material
www.sciencemag.org/cgi/content/full/332/6026/206/DC1
Materials and Methods
Tables S1 and S2
References

13 December 2010; accepted 11 February 2011
10.1126/science.1201596

Ribozyme-Catalyzed Transcription of an Active Ribozyme

Aniela Wochner, James Attwater, Alan Coulson, Philipp Holliger*

A critical event in the origin of life is thought to have been the emergence of an RNA molecule capable of replicating a primordial RNA "genome." Here we describe the evolution and engineering of an RNA polymerase ribozyme capable of synthesizing RNAs of up to 95 nucleotides in length. To overcome its sequence dependence, we recombined traits evolved separately in different ribozyme lineages. This yielded a more general polymerase ribozyme that was able to synthesize a wider spectrum of RNA sequences, as we demonstrate by the accurate synthesis of an enzymatically active RNA, a hammerhead endonuclease ribozyme. This recapitulates a central aspect of an RNA-based genetic system: the RNA-catalyzed synthesis of an active ribozyme from an RNA template.

An earlier, simpler biology might have relied on RNA for both heredity and metabolism. Evidence for such an "RNA world" (*1*) preceding modern life includes the central catalytic and informational roles of RNA in splicing, gene expression, and translation (*2*–*4*), as well as the versatility of RNA in forming specific receptors and catalysts (*5*, *6*). Organisms of the putative RNA world would have required an RNA polymerase ribozyme for both RNA-based heredity and the expression of "RNA genes." Although the ancestral replicase appears to have been lost, key functional aspects of RNA-catalyzed RNA replication can be studied "by proxy" with the use of modern ribozymes generated by in vitro selection, such as the R18 RNA polymerase ribozyme (Fig. 1A) (*7*). R18 was isolated from a random sequence pool by in vitro evolution and stepwise engineering of the initial class I ligase ribozyme (*8*–*10*). Although R18 is a general RNA polymerase, its activity is both sequence-dependent and limited to transcribing stretches of RNA up to 14 nucleotides (nt) long on a favorable RNA template (*7*). Starting from R18, we have used both RNA evolution and engineering to generate new RNA polymerase ribozymes with improved polymerase activity and sequence generality (*11*).

Compartmentalized bead-tagging. Strategies for the in vitro selection of catalytically active RNAs commonly involve the acquisition (or loss) of a capture tag for recovery (*12*, *13*). This restricts direct selection for more advanced enzymatic properties, such as multiturnover catalysis. Directed evolution of RNA polymerase ribozymes is complicated further by their poor primer extension efficiency: Substantial extension of a single primer remains a sporadic event, which reduces the effective size of polymerase ribozyme libraries. Furthermore, ribozyme repertoires must be transcribed by, for example, T7 RNA polymerase, which outperforms likely ribozyme polymerase candidates and must therefore be absent during the selective step. Finally, a sensitive and sequence-specific detection strategy is required to distinguish between simple nucleotide transferase and genuine templated polymerase activities.

We developed a selection strategy, termed compartmentalized bead-tagging (CBT), that harnesses water-in-oil emulsion technology (*14*) to link ribozyme genes to thousands of copies of the corresponding ribozyme via microbead display (fig. S1). CBT separates transcription from subsequent selective primer extension and allows the selection of clonal ribozyme populations rather than individual ribozyme molecules. The sampling of the aggregate activity of thousands of clonal ribozymes and a sensitive fluorescence signal amplification of extended primers by rolling circle amplification (RCA) (figs. S1c, S2, and S3) enable the discovery and isolation of polymerase ribozymes as a function of their primer extension capability. We validated CBT using model selections of R18 ribozyme genes spiked into an excess of inactive R18 genes (R18i) (fig. S1b), which yielded up to a 10^5-fold enrichment of active genes (fig. S1d).

Ribozyme RNA polymerase selection. We sought to improve ribozyme-primer-template interactions, known to be poor in the R18 ribozyme (*7*, *15*, *16*), by appending a random-sequence RNA domain to the 5′-end of R18, a region implicated in interactions with the primer-template duplex (*17*). A short "stem" RNA (table S1) that completes R18 by formation of a helix (P2) (*7*) was omitted from this selection as its functional relevance had been called into question (*16*).

CBT selection was applied to this library (~5×10^7 sequences) (table S2). We developed a microtiter plate–based assay (RPA, ribozyme polymerase plate assay) (fig. S4) to screen for clones of interest. After three rounds of CBT, we observed an increase in polyclonal ribozyme activity (fig. S5a) and, by RPA, identified one ribozyme (C19) with improved RNA polymerase activity among 22 clones screened (Fig. 2, A and B).

C19 differed from the parent R18 ribozyme by the presence of a new 5′-domain, as well as a single point mutation (G93A) (Fig. 1B). The G93A mutation was located in the P2 region of the ribozyme and compensated for the reduction in polymerase activity caused by the absence of the stem oligonucleotide. Indeed, the A93G back-mutation rendered C19 RNA polymerase activity stem-dependent (fig. S5b).

Secondary structure prediction of the new 5′-domain indicated that it comprised a 6-nt single-stranded sequence segment (ss_{C19}) at the 5′ end, followed by a hairpin domain (HP_{C19}). ss_{C19} showed complementarity to the 5′ end of the template (TI) that had been used for both selection and screening. Binding of ss_{C19} to the template was required for C19 activity, as templates containing successive mutations of the ss_{C19} complementary sequence showed a progressive loss in activity (Fig. 2C). Compensating mutations in ss_{C19} (to reconstitute a 6-nt hybridization site) restored activity, although not consistently to C19 levels. This suggests that ss_{C19} enhances C19 activity primarily (but not exclusively) by promoting recognition and binding of template downstream of the primer 3′ end.

Long-range RNA synthesis. Although C19 showed improved polymerase activity on the selection template TI (Fig. 2B), the activity enhancement of C19 compared with R18 was much

Medical Research Council (MRC) Laboratory of Molecular Biology, Hills Road, Cambridge CB2 0QH, UK.

*To whom correspondence should be addressed. E-mail: ph1@mrc-lmb.cam.ac.uk